



Potential of Nb₂O₅ nanofibers in photocatalytic degradation of organic pollutants

Edson Tobias de Jesus^{1,2,3} · Ailton José Moreira^{2,4} · Mayara Coelho Sá^{1,2,3} · Gian Paulo Giovanni Freschi⁴ · Miryam Rincón Joya⁵ · Maximo Siu Li⁶ · Elaine Cristina Paris¹ 

Received: 16 March 2021 / Accepted: 9 July 2021 / Published online: 23 July 2021

© The Author(s), under exclusive licence to Springer-Verlag GmbH Germany, part of Springer Nature 2021

Abstract

Various photocatalytic nanomaterials for environmental remediation have been promoted due to the pollution caused by different organic pollutants. In this study, Nb₂O₅ nanofibers were obtained by electrospinning technique, presenting controlled crystallinity and high specific surface area to improve the photoactivity response. The structural characterization indicated Nb₂O₅ nanofibers with orthorhombic phase formation. The photoluminescence measurements showed different energy levels contributing to the electronic transition events. The nanofibers with a bandgap up to 3.6 eV were applied to photocatalysis of dyes (rhodamine B (RhB) or methylene blue (MB)) and fluoxetine (FLX), listed as an emergent pollutant. In the optimized condition (pH = 9), the RhB and MB photocatalysis was 59% and 93% more efficient than photolysis due to $\zeta = -50 \text{ mV} \pm 5$ for EtOH_550 sample increased interaction with MB (cationic) compared to RhB unprotonated (pK_a = 3.7). Therefore, FLX (pK_a = 10.7) was selected due to protonated form at pH = 9 and showed $68\% \pm 1$ adsorption in 30 min for EtOH_550. The FLX photocatalytic degradation under UV light irradiation was up to 17% higher than the photolytic degradation. The formation of hydroxyl radicals in the photocatalytic system (EtOH_550) was proven by the Coumarine probe assay, corroborating with the greater amount of α -[2-(methylamino)ethyl]benzylalcohol (MAEB), a by-product obtained after FLX oxidation. Additionally, the material achieved specific catalytic activity for the different organic compounds (RhB, MB, or FLX). Therefore, Nb₂O₅ nanofibers were efficient for degrading three different pollutants under UV light, proving a viable alternative for environmental remediation.

Keywords Photocatalysis · Organic pollutant · Drug · Ceramic nanofiber · Electrospinning

Responsible Editor: Sami Rtimi

✉ Elaine Cristina Paris
elaine.paris@embrapa.br

¹ Nanotechnology National Laboratory for Agriculture (LNNA), Embrapa Instrumentação, XV de Novembro St., 1452, zip code, São Carlos, SP 13560-970, Brazil

² Department of Chemistry, Federal University of São Carlos, Rod. Washington Luiz, km 235, zip code, São Carlos, SP 13565-905, Brazil

³ Federal Institute of Education, Science and Technology of Maranhão, Baronesa street, zip code, Alcântara, MA 65250-000, Brazil

⁴ LAFPEQ, Institute of Science and Technology, Federal University of Alfenas, UNIFAL-MG, Poços de Caldas, MG 37715-400, Brazil

⁵ Departamento de Física, Universidad Nacional de Colombia, Calle 45 #30-03, Bogotá C.P. 111321, Colombia

⁶ Institute of Physics, University of São Paulo, São Carlos, SP 13563-120, Brazil

Introduction

Pollution resulting from the inappropriate disposal of the varied industrial waste types has been the main route for contamination of environmental ecosystems (Kostich et al. 2014; Pinheiro et al. 2016; Lee et al. 2017). With the advancement of fine chemistry, new molecules have been created to meet society's demands in food (Kuenemann et al. 2017), health (Farooqui et al. 2018), agriculture (Sanaullah et al. 2020), and social well-being fields. Consequently, these new molecules have been increasingly introduced into ecosystems as contaminants, affecting environmental quality and increasing human health risks (Gouvêa et al. 2018; Grenni et al. 2018). Among these, new molecules with high polluting potential stand out in the class of dyes, pesticides, and pharmaceutical products (Lapworth et al. 2012; Malafatti et al. 2020). However, considering that environmental legislation does not keep up the speed with which these new molecules are created, this type of pollutant regulation is limited or non-existent in many

countries (Petrie et al. 2015; Gorito et al. 2017). Watchful of this new reality, the scientific community has found in nanotechnology the appropriate tools to minimize this type of pollution (Khan and Tahir 2019; Paris et al. 2020). In this sense, advanced oxidation technologies, especially heterogeneous photocatalysis, have been the most efficient tools to remove these emerging contaminants from environmental ecosystems (Védrine 2019).

The photocatalytic mechanism responsible for the degradation of organic pollutants is widely known. It can be summarized in the ability that materials with semiconductor properties exhibit to generate oxidizing (h^+) and reducing (e^-) sites on their surface (Rauf and Ashraf 2009; Gurgel et al. 2011). Therefore, when absorbing a photon, these materials promote the electron from the valence band (VB) to the conduction band (CB), giving rise to the electron/hole pair responsible for triggering the redox reactions (Oliveira et al. 2013; Shen et al. 2019). According to the literature, photocatalytic success is associated with the electronic photoexcitation efficiency, recombination processes decrease, active surface increase, the interaction between molecule/catalyst, and catalyst homogeneity in the reaction system (Fang et al. 2017; Moreira et al. 2020a). Furthermore, this property is also broadly correlated with the ceramic material crystalline structures (Paris et al. 2010), which can be influenced by the synthesis method (Leite et al. 2000) and heat treatment temperature (Alves et al. 2009). Therefore, TiO_2 application as a photocatalyst has been extensively investigated for environmental remediation. Nowadays, its physical-chemical modification has been proposed to optimize these processes (Shen et al. 2019). However, the search for alternative materials to TiO_2 has promoted significant advances in the field of heterogeneous photocatalysis, where semiconductors based on niobium oxide have been gaining prominence (Nico et al. 2016).

Nb_2O_5 as a photocatalyst for environmental remediation is still little reported than other semiconductors such as TiO_2 and ZnO . However, its photoactivity has shown to be promising (Raba et al. 2015; Falk et al. 2017). The Nb_2O_5 structural properties favor chemical oxidation due to its ability to diffuse surface oxygen to form the reactive species $\cdot O_2^-$ and $\cdot OH$ (Nico et al. 2016). Moreover, the Nb_2O_5 surface characteristics highlight its adsorptive properties, favoring chemical conversions (Zhuang et al. 2016). By comparing the TiO_2 and Nb_2O_5 photoactivity, the niobium oxide electronic structure transitions are more varied, selecting its application in photocatalytic processes (Nb et al. 2018).

Thus, different synthesis methods have been investigated to obtain Nb_2O_5 (Nogueira et al. 2017; Falk et al. 2017; Silva et al. 2019). The precipitation method by dissolution in an aluminum reduction system supplied Nb_2O_5 in rod forms was evidenced for $H_2(g)$ production in a photocatalytic process (Zhao et al. 2016). Additionally, the evaporation-induced self-assembly (EISA) (Hashemzadeh et al. 2014), oxidant

peroxide (Lopes et al. 2014), microwave-assisted (Falk et al. 2017), and polymeric precursors (Raba et al. 2015) methods were also applied to obtain Nb_2O_5 as a photocatalyst. When used for photocatalytic degradation of different organic pollutants, the efficiency is in the order of 45% for atrazine in 30 min (Lopes et al. 2014), > 95% for MB in 50 min (Shao et al. 2014), and > 45% for MB in 120 min (Falk et al. 2017). As an unconventional synthesis method, the electrospinning technique was applied to synthesize Nb_2O_5 nanofibers, exhibiting good performance to produce nanomaterials with structural defects that favor electromigration (Grishin et al. 2013). This method also exhibited Nb_2O_5 with small particle diameters (21 to 37 nm) and a high specific surface area (Leindecker et al. 2014). The Nb_2O_5 nanofiber photoactivity response was evaluated to the methyl orange degradation, reaching 62% in 3 h (Qi et al. 2013).

Under specific heat treatment conditions, the textural properties of Nb_2O_5 fibers can be controlled to become efficient adsorbents for organic molecules (Ferreira et al. 2019). The adsorption process between nanomaterials and different compounds is responsible for optimizing the interaction between the nanomaterial and a specific molecule (Pi et al. 2018). The literature has already shown the different compound chemical nature influences in the photocatalytic process efficiency since their protonated/deprotonated form guides the material/molecule interaction (Bian et al. 2011). Thus, anionic/cationic dyes or molecules with different lipophilicity degrees can show distinct efficiency for the same catalyst during the photocatalytic process (Wang et al. 2013, 2014). This aspect implies that the material photoactivity cannot be discussed just because of their physical-chemical properties but must be associated with the compound chemical nature to be degraded.

Materials that exhibit surfaces with a high density of negative charge can optimally disperse the reaction system, increasing the active area and degradation efficiency (Pi et al. 2018). On the other hand, however, these same materials can repel negatively charged molecules, decrease surface interaction, and impair photocatalytic efficiency (Bian et al. 2011). Therefore, in the photocatalysis field, deepening investigations about the pollutant chemical nature and its interaction with nanomaterial can optimize photocatalytic processes.

In this study, Nb_2O_5 nanofibers were efficiently obtained after optimizing the electrospinning method proposed in the literature (Leindecker et al. 2014). The nanofiber photocatalytic activities were monitored for the RhB and MB dyes and the FLX drug (emerging pollutant) degradation, chosen for the chemical nature (MB = cationic, RhB $pK_a = 3.7$, and FLX $pK_a = 10.7$). Also, the FLX degradation and some of its by-products were accompanied by high-performance liquid chromatography (HPLC), which provided important information regarding the degradation mechanism mediated by Nb_2O_5 nanofibers. Details apropos the dye degradation mechanism in this study show the importance of seeking a new statement

on the Nb₂O₅ ceramic fibers application for environmental remediation. Thus, expanding studies on the material capacity to form reactive oxygen species influenced by parameters such as the reaction medium pH, the adsorption process contribution, and the degradation of different organic contaminants are a novelty.

Experimental

Nb₂O₅ ceramic nanofibers preparation

Nb₂O₅ ceramic nanofibers were prepared by the electrospinning technique (Leindecker et al. 2014). Briefly, an alcoholic solution (10% w v⁻¹) of polyvinylpyrrolidone (PVP) was prepared using ethanol (EtOH) and methanol (MeOH). These organic solvents were selected to achieve the PVP solubility and the appropriate viscosity of the polymeric precursor. Solution viscosity was maintained between 45 to 65 cP. Then, niobium ammonium oxalate (NAO) was added to a polymeric solution in the ratio of 2:1 PVP/NAO (w:w) in 1 mL of acetic acid with a viscosity of 45–65 cP. After complete solubilization, 15 mL of polymeric blend solution (PVP/alcohol/NAO) was kept under stirring for 12 h. Then, 5 mL of blend solution was transferred into a 10-mL glass syringe with a 0.7-mm diameter metal rod needle. A metallic cylindrical collector was covered with aluminum foil at a distance of 10 cm from the needle tip and kept under rotation for ceramic blanket formation. Here, a metal needle was connected to the electric system and submitted at a voltage of 26 kV. Simultaneously, the collector was grounded to close the electrical circuit, and the solution flow rate was maintained at 1.6 mL h⁻¹. After 40 min, the blanket form composite was collected and dried at 80 °C for 12 h in the oven for solvent remotion. Finally, the blankets were calcined at 550 °C for 4 h and 600 °C for 3 h in a traditional muffle furnace with 2 °C min⁻¹ of heating/cooling rates. According to solvent and the thermal treatment temperature, the obtained Nb₂O₅ ceramic fibers were named EtOH_550, EtOH_600, MeOH_550, and MeOH_600.

Characterization assays

The viscosity of the polymeric blend solution was measured by Brook Field viscometer. The thermal behavior of composite fibers was evaluated using TA Instruments equipment (model SDT 650). Approximately 20 mg of each sample was transferred to the alumina crucible and heated from 30 to 1000 °C with a 10 °C min⁻¹ heating rate, under 100 mL min⁻¹ synthetic airflow. Structural characterization was done by X-ray diffraction (XRD), using a Shimadzu XRD 6000 diffractometer (Cu-Kα/λ = 1,5406 Å), 30-kV operating voltage, 30-mA tube current, 10–85° angular scan (2θ interval),

and 0.02° min⁻¹ dislocation. Crystallite size was calculated using the Scherrer equation (Hargreaves 2016), and the lattice parameters obtained using Bragg's law (Stern 1978). Raman spectroscopy was applied to evaluate the nanofiber crystalline structures in the short-range order. The assays were realized by a Renishaw spectrophotometer (model RM 2000) with backscattering in the region of 100–4000 cm⁻¹, an argon laser of 1 μm² area, and a wavelength spot 632.8 nm as the excitation source. Nanofiber morphologies were characterized by Field Emission Gun Scanning Electron Microscopy (FEG-SEM) using a Jeol microscope (model JSM-6701F). Moreover, the presence of functional groups on the material surface was analyzed by Fourier transform infrared spectroscopy (FTIR) using a Bruker Equinox 55 spectrometer. The spectra were obtained between 4000 and 400 cm⁻¹, adjusted in the transmittance module, 4 cm⁻¹ resolution, and 32 scans. Zeta potential was obtained using a Zetasizer nano-ZS analyzer (Malvern Instruments, UK) with dropwise addition of 0.1 mol L⁻¹ HCl or NaOH solution for pH = 1 to 10 adjustment. Nitrogen (N₂) adsorption and desorption analyses were performed by the Brunauer, Emmett, and Teller (BET) method on Micromeritics equipment (ASAP 2000 model). A 160 mg of sample was oven-dried at 80 °C for 12 h under vacuum and subsequently evacuated at a rate of 1.36 × 10⁻³ bar s⁻¹ for 60 min. The samples were analyzed by applying a heating rate of 10 °C min⁻¹ up until 200 °C. The material optical properties were investigated by diffuse reflectance spectroscopy (DRS) in the UV-Vis region. The data were obtained on a UV-Vis spectrophotometer (Shimadzu, UV-2600) in the range of 200 to 800 nm. The Kubelca-Munk equation was used to calculate the bandgap of the material (Kumari et al. 2020). Additionally, photoluminescence (PL) measurements on the solid samples were performed using a spectrometer model QE65000 (Ocean Optics), with excitation at λ = 405 nm and 100 mW laser power. The emission was collected in the 450- to 800-nm range. The PL band best adjustments were obtained by the Voigt equation area (McPhie 2000).

Photolytic and photocatalytic assays

The photolytic and photocatalytic assays under UV (254 nm, 0.94 mW cm⁻²) light were performed in a reactor described in the literature (Moreira et al. 2018), with temperature control at 18 °C. Photocatalytic assays evaluated catalytic activity for MB and RhB dyes and the FLX.

Dyes photodegradation

Three milligrams per liter (9.4 μmol L⁻¹) MB or 5 mg L⁻¹ (10 μmol L⁻¹) RhB solutions were prepared by dissolving the reagent (98%, Synth) in ultrapure water. For the photocatalytic assay, 10 mg of the Nb₂O₅ nanofibers were added to a glass

beaker and dispersed in 20 mL of the MB or RhB solution under constant stirring. Samples were stirred for 0.5 h (MB) or 12 h (RhB) in the dark for prior adsorption. After that, samples were irradiated for 5 h (RhB) and 90 min (MB). At each time interval, an aliquot of the sample was collected and analyzed by molecular absorption. After analysis, the samples were returned to the beaker for the new irradiation interval to keep the constant volume. Molecular absorption spectra of the dyes were scanned in the 200- to 800-nm range using a Shimadzu -1601PC spectrophotometer.

Also, a reuse study of up to 4 cycles was applied to evaluate the extended photoactivity of the catalyst that showed better performance. Therefore, the material recovered after each cycle was washed with distilled water (1 time), pure ethanol (2 times), and dried at 60 °C for 12 h, before a new application of 300 min for RhB and 90 min MB.

FLX photodegradation

N-Methyl-3-phenyl-3-[4-(trifluoromethyl)phenoxy]propan-1-amine (FLX) (98%, Santa Cecilia pharmacy), 4-trifluoromethyl phenol (TFMP), α -[2-(methylamino)ethyl]benzylalcohol (MAEB), and 3-phenylpropyl methylamine (PPMA) solutions were separately prepared by dissolving the pure reagents (all > 97%, Sigma-Aldrich) in ultrapure water. Then, 10 mg L⁻¹ (32 μ mol L⁻¹) of FLX solution was applied in the photocatalytic assays. At the same time, TFMP, MAEB, and PPMA were used for calibration curve preparation by HPLC with UV-Vis detection (205 nm). FLX, MAEB, PPMA, and TFMP were monitored through retention times (min), previously calibrated with standard solutions of the pure reagents. More details on the analytical methodology and solution preparations can be obtained from the literature (Moreira et al. 2020a). For the photocatalytic assay, in a 50-mL beaker and 4.2-cm top opening diameter, 5 mg of the Nb₂O₅ nanofibers was dispersed in 10 mL of FLX solution (10.0 mg L⁻¹) under constant stirring and kept in the dark for 30 min. Then, samples were irradiated in the time interval of 3 to 120 min, filtered in the 0.22- μ m membrane for catalyst removal, and subjected to chemical analysis by HPLC. Finally, dye or FLX solutions with pH-adjusted were obtained by dropwise addition of 0.1 mol L⁻¹ HCl or NaOH solution and monitored by a potentiometer coupled to a glass membrane electrode. Hydroxyl radical probe assay was performed following the literature method (Moreira et al. 2020b).

Results and discussion

Structural characterization

X-ray diffraction patterns of the Nb₂O₅ ceramic fibers were indexed according to JCPDS 30-0873 (Fig. 1). The highest intensity peaks were observed at $2\theta = 22.7^\circ$, 28.5° , and 36.7°

attributed to the orthorhombic phase (T-Nb₂O₅) (Zeng et al. 2017). The intense and well-defined lines (001), (180), and (181) showed the crystalline nature of the materials that was influenced neither by solvents (MeOH or EtOH) nor by heat treatment temperature (550 or 600 °C). These results corroborated the higher thermal stability of the ceramic material above 550 °C (Fig. S1). Furthermore, due to a mass loss above 90% for the polymeric blanket by successive thermal events, a complete elimination of organic matter according to the infrared spectra (Fig. S2) was observed. This study revealed that the confirmation of Nb₂O₅ ceramic fiber crystalline behavior agrees with the literature (Nowak and Jaroniec 2008; Leindecker et al. 2014).

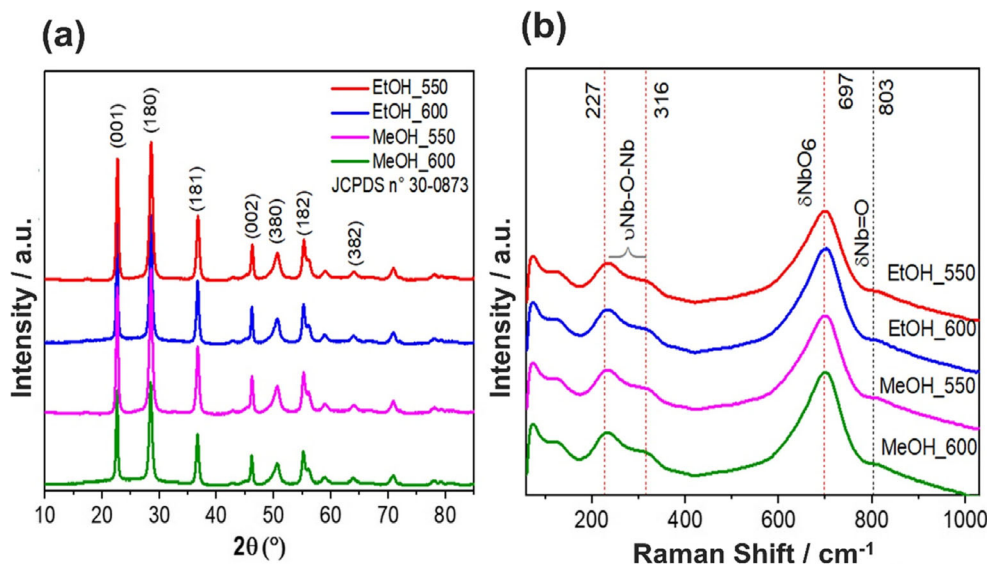
Figure 1b shows the Raman shifts for Nb₂O₅ ceramic materials. The angular vibrations ν (Nb-O-Nb) between peaks 227 and 316 cm⁻¹ were assigned to the NbO₄ tetrahedron. Peaks at 697 cm⁻¹ were attributed to the δ (Nb-O) symmetrical stretches of the (NbO₆⁻⁷; NbO₇⁻⁹; NbO₈⁻¹¹) polyhedra, and the peak at 803 cm⁻¹ was ascribed to the symmetrical stretching of the δ (Nb = O) surface group (Lopes et al. 2014; Hossain et al. 2019). The Raman spectra corroborate to XRD, showing the Nb₂O₅ orthorhombic phase exclusively in all samples. The unit cell parameters (a, b, and c) were calculated for EtOH_550, EtOH_600, MeOH_550, and MeOH_600. The average value of the four samples was (a) = 6.24 Å ± 0.01, (b) = 28.94 Å ± 0.04, and (c) = 3.93 Å ± 0.01, showing the similarity between them. When comparing the average values of (a), (b) and (c) with those reported in JCPDS 30-0873, the approximation was 99% (a), 101% (b), and 100% (c). Thus, the results of structural characterization confirm that the orthorhombic phase with high crystallinity was obtained for all samples, and therefore, the application in heterogeneous photocatalysis shows potential since the literature has already confirmed the T-Nb₂O₅ photoactivity (Lopes et al. 2014; Shao et al. 2014).

Morphological characterization

Figure 2 showed the FEG-SEM images of the EtOH_550, EtOH_600, MeOH_550, and MeOH_600 samples, confirming the Nb₂O₅ nanometric fibers (< 90 nm). In the current study, the fiber diameter was reduced by 40% compared to the similar synthesis method used to produce Nb₂O₅ (Leindecker et al. 2014). This characteristic is preferred in photocatalysis studies since materials with a smaller diameter show a superior surface area.

According to Table 1, the average sample diameters treated at 550 °C were 35% smaller than the treated at 600 °C. However, the samples processed in EtOH (550 and 600 °C) showed a fiber diameter of 15% smaller, concerning the samples processed in MeOH under the same temperature conditions. These results indicated that the methanol (MeOH = 64 °C), the lowest boiling point solvent, is volatilized more

Fig. 1 XRD patterns (a) and Raman spectrum (b) of the Nb₂O₅ nanofibers



efficiently than ethanol (EtOH = 78 °C), favoring the Nb₂O₅ crystal agglomeration. However, this same heat treatment temperature did not significantly influence the crystallites size (Table 1). Thus, the fiber diameter increased due to the particle agglomeration degree obtained after the polymeric structure decomposition.

Samples processed with EtOH showed a surface with homogeneous roughness (inset) and without holes (Fig. 2b).

Therefore, the Nb₂O₅ growth and particle organization occurred more homogeneously to form the ceramic fibers. On the other hand, as MeOH is the most volatile, the obtained fibers with these solvents showed superficial deformations (Fig. 2d) and small holes distributed heterogeneously along with the structure (inset). Consequently, ceramic fibers with large SSA values were obtained, increasing the material potential for heterogeneous photocatalysis.

Fig. 2 FEG-SEM images of the Nb₂O₅ nanofibers obtained at different solvents and calcined at 550 °C for 4 h or 600 °C for 3 h

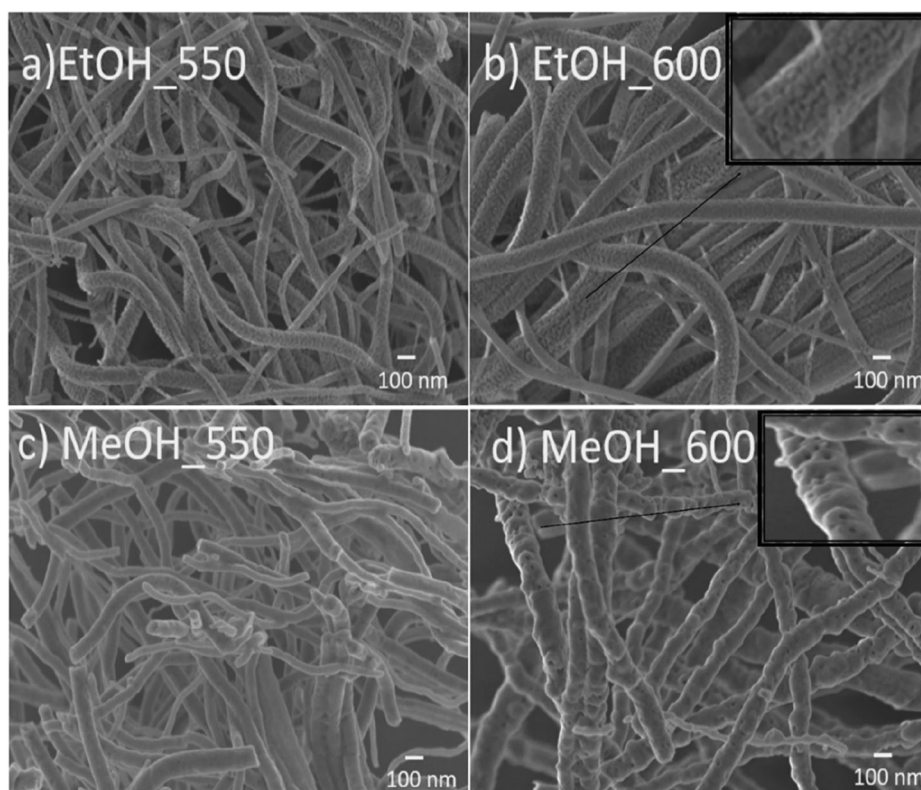


Table 1 Crystallite diameter calculated according to the Scherrer method, fiber diameter obtained by measuring n counts ($n = 100$) of the FEG-SEM images and BET surface area

Sample	Crystallite diameter* (nm)			Fiber diameter (nm)	Area BET ($\text{m}^2 \text{g}^{-1}$)
	(001)	(180)	(181)		
EtOH_550	18.78	13.96	15.22	47.0 ± 0.7	37.4 ± 0.4
EtOH_600	24.00	15.14	16.04	72.0 ± 0.5	37.8 ± 0.4
MeOH_550	19.09	13.56	14.49	56.0 ± 0.7	40.5 ± 0.6
MeOH_600	22.79	14.16	15.22	85.0 ± 1.7	32.6 ± 0.3

*Scherrer diameter

Optical characterization

The optical property of the Nb_2O_5 fibers was investigated by diffuse reflectance analysis. The direct bandgap energy was calculated according to the literature (Lopes et al. 2014). For all samples, the diffuse reflectance spectrum exhibited a homogeneity that corroborates with the XRD data, showing a single crystalline phase ($\text{T-Nb}_2\text{O}_5$). Consequently, the average bandgap energy was $E_g = 3.87 \text{ eV} \pm 0.04$ for MeOH_550, MeOH_600, and EtOH_600 samples. The EtOH_550 showed an $E_g = 3.6 \text{ eV}$ slightly shifted to the lower energy. Therefore, the Nb_2O_5 fiber photoactivity investigation viewing heterogeneous photocatalysis applications requires ultraviolet wavelength.

Figure 3 shows the PL spectra with top emission centers. The area percentage of each profile was adjusted using the Voigt (area) function, as described in the “Characterization assays” section. All PL profiles are broadband type, showing an evident relationship between the contributions of various energy levels to the electronic transition process. The Nb_2O_5 fiber bandgap values were higher than the maximum PL emission of each sample (~ 2.3 to 2.6 eV) at 477 to 545 nm, respectively (Fig. 3a). Therefore, broad PL spectra cover part of the visible electromagnetic spectrum, while band-to-band electronic transitions slightly influence. This optical phenomenon may be related to the prohibited zone’s additional energy

levels due to the surface, interface, and bulk defects (Paris et al. 2007; Machado et al. 2017).

The differences observed in each PL spectra were treated individually with the insertion from three to six Voigt peaks, perfectly adjusted to the spectrum, as shown in Fig. 4. In all cases, a broadband emission profile in which the maximum emission, intensity, and amplitude were significantly dependent on the heat treatment temperature and solvents used in the fiber processing. Initially, there was a trend, with respect to the heat treatment variation in relation to the PL intensity ($\text{PL}_{\text{MeOH}_550} > \text{PL}_{\text{EtOH}_550} > \text{PL}_{\text{EtOH}_600} > \text{PL}_{\text{MeOH}_600}$).

The samples treated at $550 \text{ }^\circ\text{C}$ for 4 h showed higher PL intensity than those treated at $600 \text{ }^\circ\text{C}$ for 3 h, which was expected due to the higher particle ordination at a higher temperature and consequent decrease in defects. For the MeOH_550 sample (Fig. 4a), the PL spectrum showed broadband and the highest intensity, with a maximum centered at 507 nm ($E_g = 2.44 \text{ eV}$) in the green color. The broadband emission of the MeOH_600 sample (Fig. 4b) showed a maximum at approximately 545 nm ($E_g = 2.27 \text{ eV}$), resulting in green color. This profile was the broadest of the samples analyzed, covering the most extensive spectrum from 450 to 750 nm. This effect on the PL spectrum may be due to a maximum amount of defects (surface, interface, and bulk) induced by structural changes (Phase $\text{TT-Nb}_2\text{O}_5$ to $\text{T-Nb}_2\text{O}_5$).

Fig. 3 Variation of $(\alpha h\nu)^2$ versus $h\nu$ for direct bandgap transitions (a) and PL spectra (b) of the Nb_2O_5 nanofibers

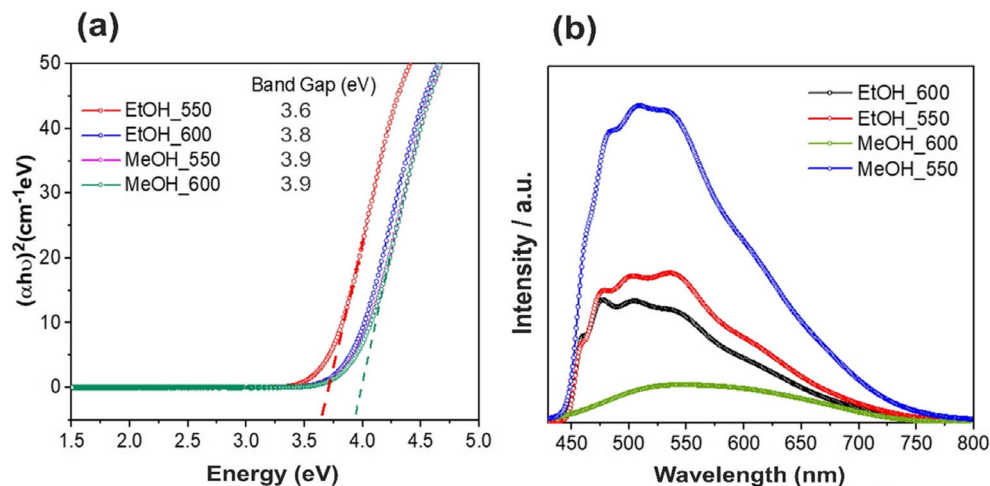
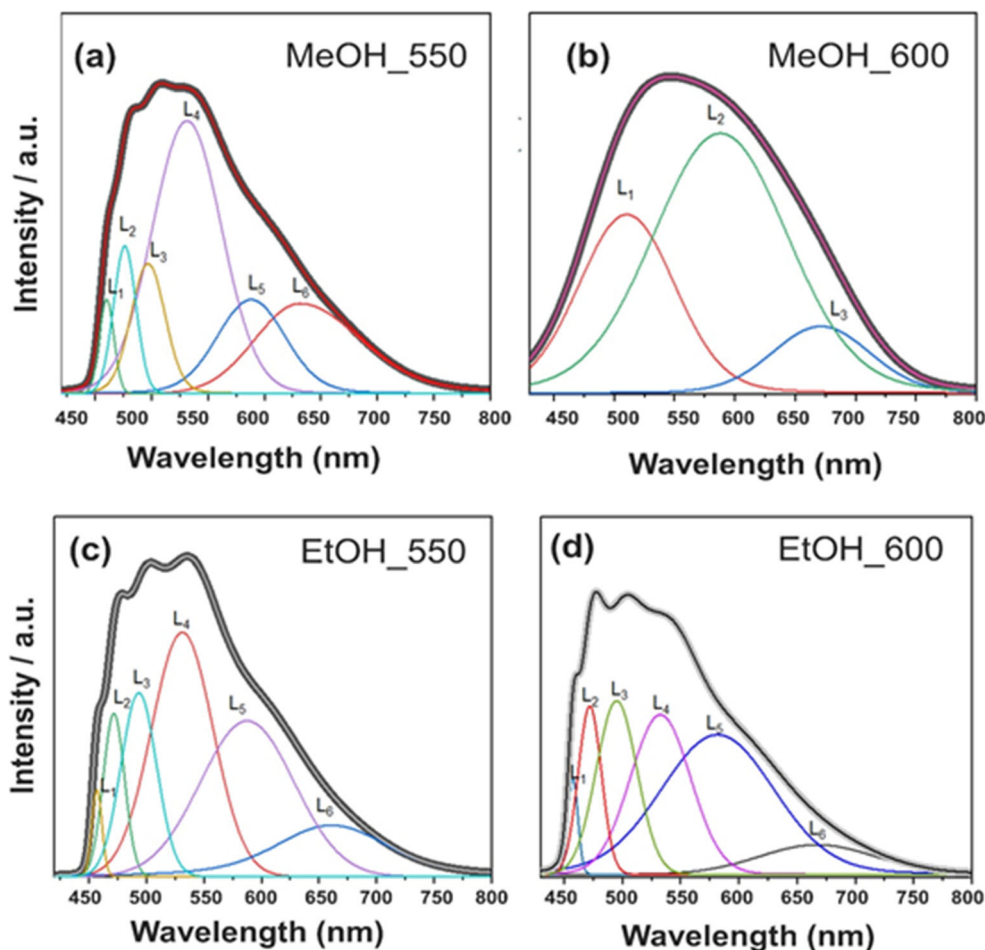


Fig. 4 PL spectra for samples MeOH_550 (a), MeOH_600 (b), EtOH_550 (c), and EtOH_600 (d)



The Nb₂O₅ orthorhombic phase begins to crystallize at 500 °C (Nico et al. 2016). In this temperature vicinity, defects from atomic diffusion, plane displacements, and NbO₆ octahedral distortion are susceptible. These changes were possibly responsible for showing a greater PL for the MeOH_550 than the MeOH_600 sample, in whose temperature more significant structural ordering was expected and consequent decrease in defects (Zhou et al. 2008; Joya et al. 2017).

However, samples processed with ethanol showed PL spectra with smaller intensity, following the same trend as those processed with methanol. Although the EtOH_550 (Fig. 4c) showed a PL minor intensity profile than MeOH_550, the first one also showed a green color broadband spectrum with a maximum of 535 nm ($E_g = 2.31$ eV). This same profile was observed for EtOH_600 (Fig. 4c). However, the PL intensity was slightly lower than observed for EtOH_550. Therefore, the PL spectra changes were evidenced by processing changes in the precursors, solvents, or temperature. Finally, Nb₂O₅ fibers were evaluated to remove organic pollutants (dye and pharmaceuticals) through heterogeneous photocatalysis under UV radiation (254 nm).

Photocatalytic activity

Photocatalytic degradation of dyes

The adsorption assays (on dark) performed for RhB (12 h) and MB (0.5 h) showed that while RhB adsorption was only 1%, MB reached 18% efficacy for the different nanofibers. According to the literature, these results were shown more significant MB adsorption than RhB when other nanomaterials were applied (Choi et al. 2015; Radoń et al. 2019). Thus, after the adsorption equilibrium, the dyes were subjected to photocatalytic assays under UV light. The degradation curves were shown in Fig. 5.

The average RhB photocatalytic degradation was $47\% \pm 2$ for Nb₂O₅ fibers in 5 h (Fig. 5a), highlighting that the EtOH_550 showed the best performance (49%). Only 10% of RhB was degraded in the photocatalyst absence, confirming the tendency. The MB photocatalytic degradation was up to $78\% \pm 1$ in 90 min for EtOH_550 (Fig. 5b), while the photolysis removed only 2%. First-order kinetic constants were calculated for all processes and depicted in Table 2.

The kinetic constants for all Nb₂O₅ fibers are shown in Table 2, confirming photocatalytic activity against RhB and

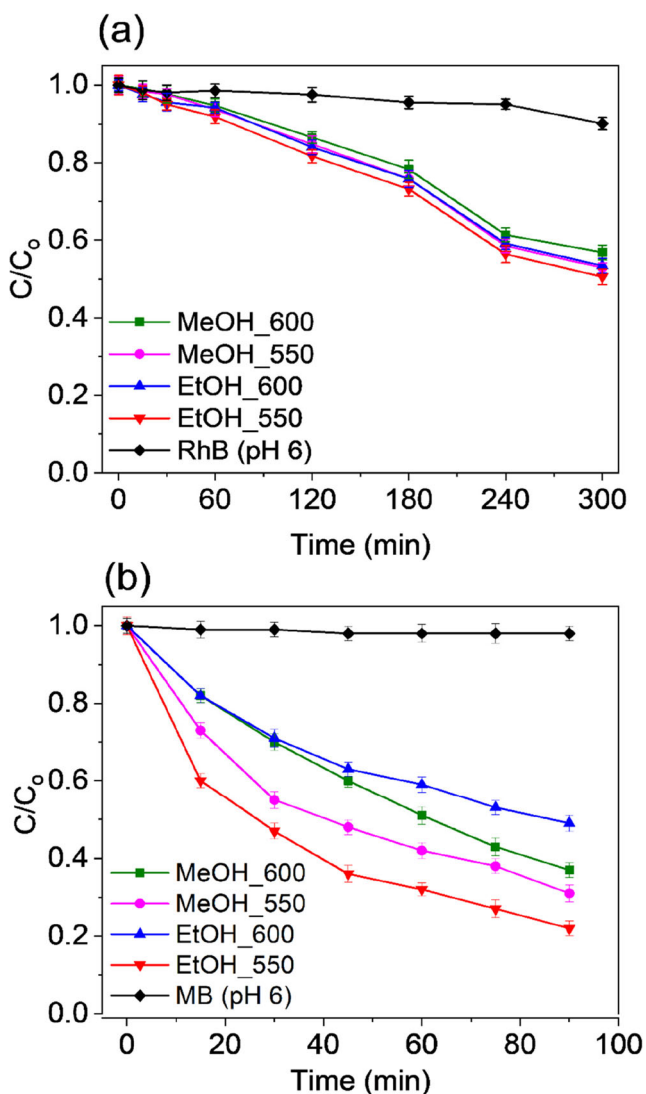


Fig. 5 Decay curves of the RhB (a) and MB (b) after photolytic or photocatalytic degradation

MB degradation. EtOH_550 efficiency was highlighted due to the highest kinetic constants for RhB ($1.77 \times 10^{-3} \text{ min}^{-1} \pm 0.06$) and MB ($12.9 \times 10^{-3} \text{ min}^{-1} \pm 0.7$). The best performance for EtOH_550 corroborates with the smaller fibers diameter, large surface area, and reduced bandgap (Tables 1 and

Table 2 First-order kinetic constants for RhB and MB

Sample	RhB $k \times 10^{-3} \text{ (min}^{-1})/R^2$	MB $k \times 10^{-3} \text{ (min}^{-1})/R^2$
Photolysis	$0.17 \pm 0.04/0.848$	*
EtOH_550	$1.77 \pm 0.06/0.996$	$12.9 \pm 0.7/0.987$
EtOH_600	$1.55 \pm 0.12/0.983$	$6.7 \pm 0.4/0.986$
MeOH_550	$1.61 \pm 0.08/0.992$	$10.5 \pm 0.8/0.974$
MeOH_600	$1.43 \pm 0.07/0.992$	$10.7 \pm 0.1/0.999$

*Due to insignificant removal, the slope was not obtained

2). When comparing the highest kinetic constants obtained for RhB and MB, an average increase of $84\% \pm 3$ was confirmed. Confirmed the best performance for EtOH_550 against the RhB and MB degradation, this material was selected for the study of reuse of up to 4 cycles. Figure 6 shows that the RhB and MB removal after the 4 cycles were $45\% \pm 3$ and $74\% \pm 2$, respectively. Simultaneously, the slight variation observed in the removal (%) after each cycle can be attributed to the minor material loss after the successive transfers. Therefore, these results indicate the maintenance of the EtOH_550 catalytic activity even after 1200 min for RhB and 360 min for MB.

Notably, the EtOH_550 performance was very different for the degradation of the different dyes in the investigated condition ($\text{pH} = 6$), suggesting that its performance was not associated with the material physicochemical properties. Thus, this enhanced catalytic performance of the fibers associated with the dye's chemical nature may have been the factor responsible for influencing the process efficiency. As the RhB charge can be changed by the $-\text{COOH}$ group protonation/deprotonation, the influence of pH was investigated.

pH evaluation

RhB and MB are cationic dyes that negative charge nanoparticle surfaces can attract to optimize the photocatalytic processes. However, only RhB presents a carboxylic acid group that can be deprotonated and increases the negative charge density in this molecule at $\text{pH} > \text{pK}_a = 3.7$ (Obregón and Colón 2013; Aguilar et al. 2014). Then, the RhB (5 mg L^{-1}) and MB (3 mg L^{-1}) solutions were evaluated respectively for 5 h and 1.5 h to investigate the photocatalytic response at different pH conditions ($\text{pH} = 3, 6, \text{ or } 9$), using EtOH_550 sample (Fig. 6).

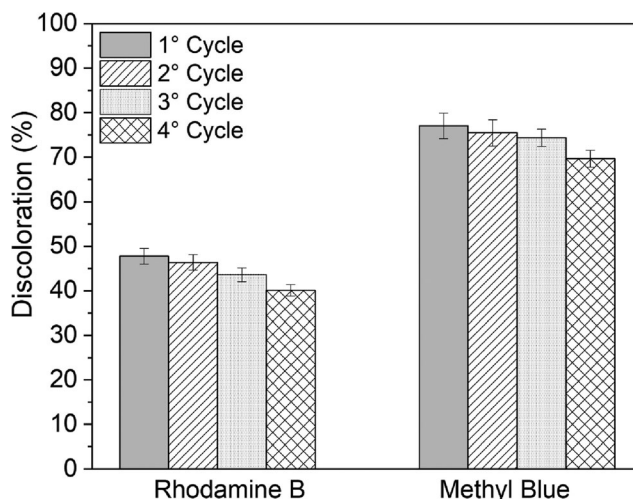
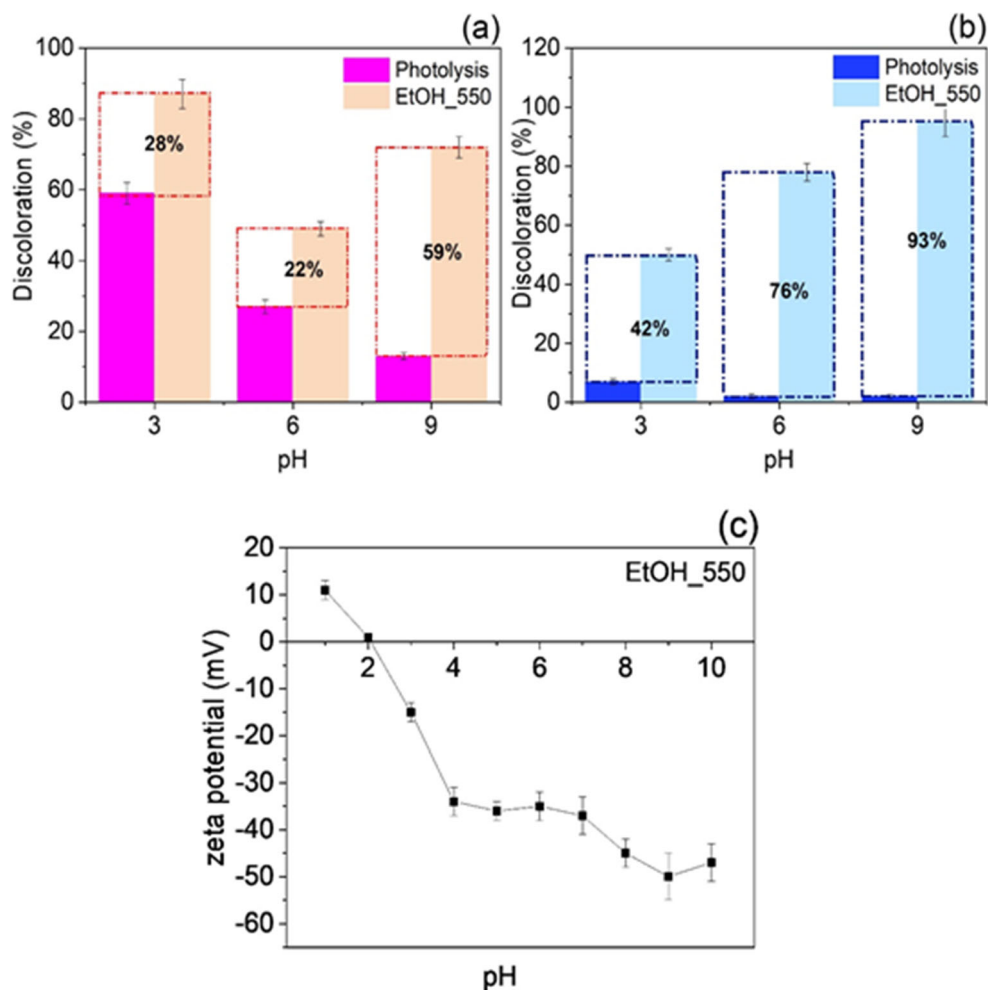


Fig. 6 RhB and MB photocatalytic removal in 4 application cycles with EtOH_550 recovered. Conditions: ($\text{pH} = 6$, degradation time: 300 min (RhB), 90 min (MB))

Fig. 7 Photocatalytic discoloration of RhB for 5 h (a) and MB for 1.5h (b) at pH = 3, 6, or 9. Zeta potential values measured at pH = 1 to 10 (c)



According to Fig. 7, the photocatalytic process was efficient for RhB and MB degradation in all pH conditions. When $pH \sim pK_a = 3.7$, RhB molecules transit in their protonated or neutral form, facilitating the interaction with oxidizing species responsible for the dye degradation (Obregón and Colón 2013). In alkaline conditions, the $-COOH$ group deprotonation increases the dye lipophilicity and significantly decreases the degradation rate (Aguilar et al. 2014). However, catalyst presence showed the best response for RhB degradation results under very different pH conditions (Fig. 7a). The RhB removal was 87% for $pH = 3$ and 72% for $pH = 9$. In comparison, the photocatalytic process performance was increased up to 28% and 59% concerning photolytic, respectively. This performance observed for the RhB photocatalytic degradation at alkaline pH was similar for MB degradation under the same conditions (Fig. 7b).

On the other hand, MB photolytic degradation was insignificant at 6 and 9 pH. Simultaneously, the addition of the EtOH_550 catalyst showed performance up to 76% for $pH = 6$ and 93% for $pH = 9$ compared to the photolytic process. Therefore, Nb_2O_5 fibers were essential to MB efficient

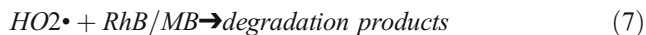
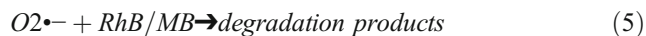
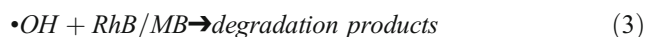
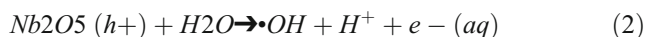
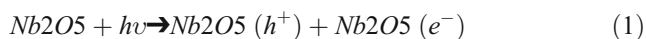
degradation, confirming the effectiveness as a catalyst for the dye degradation process.

In contrast to the RhB, the MB does not show the $-COOH$ group affected by the acid-base equilibrium reaction, presenting a strictly cationic molecular structure. This aspect draws attention to the dissimilar performances, suggesting that the different dye charge distribution was the parameter responsible for optimizing the degradation process in an alkaline pH. Therefore, to better understand the pH influence in the photocatalytic process, the zeta potential of the EtOH_550 fibers was measured in the $pH = 1$ to 10 range (Fig. 7c). The zero charge point was identified at $pH \sim 2$, while the negative charge surface was confirmed in all pH conditions > 2 .

At $pH = 3$, RhB is protonated ($pK_a = 3.7$), optimizing the interaction with the EtOH_550 fiber which showed a slightly negative charge ($\zeta = -15 \text{ mV} \pm 1$). At $pH = 9$, the EtOH_550 fiber showed a significantly negative charge ($\zeta = -50 \text{ mV} \pm 5$) capable of repelling the deprotonated RhB (Merka et al. 2011). Even with the less interaction between RhB and EtOH_550 at $pH = 9$, the photocatalysis efficiency was confirmed, showing that $\zeta = -50 \text{ mV} \pm 5$ could optimize the

EtOH_550 fiber dispersion, increasing the active area. This justification is applied to the efficient MB degradation at pH = 9, optimized due to the better fiber dispersion in the reaction medium. The -COOH group absence in the MB allowed the photocatalytic degradation to be 93% against the 59% observed for RhB. These RhB and MB photocatalytic degradation results follow the literature, showing the organic pollutant chemical nature is an important factor in understanding the photodegradation mechanism (Merka et al. 2011; Obregón and Colón 2013; Reeta Mary et al. 2018). Also, this increase of the negative material charge in less acidic conditions occurred due to the probable deprotonation of Nb-O groups identified by Raman analyses (Fig. 1), corroborating with the literature (Silva et al. 2019).

To clarify the Nb₂O₅ photocatalytic mechanism for dye degradation, the set of Eqs. (1) to (7) summarizes the reactions (Rtimi et al. 2018).



Due to the best response for dye photocatalytic degradations using EtOH_550 at pH = 9, this catalyst and conditions were applied to degrade FLX. This pharmaceutical product choice was due to the high pKa = 10.7 (Do et al. 2017), which preferably shows its protonated form at pH = 9 and possibly a better interaction with EtOH_550, which led to a $\zeta = -50 \text{ mV} \pm 5$. However, the -CF₃ group presence in the FLX molecular structure shows a negative charge density that can compete with the contribute repulsion from catalyst even for the protonated system. Thus, the photocatalytic degradation of FLX was investigated.

FLX photocatalytic degradation

A 10 mg L⁻¹ FLX solution (pH = 9) was subjected to adsorption with EtOH_550 in 1- to 30-min range (Fig. 8a). The results showed adsorption > 85% ± 2 in 1 min, indicating a rapid interaction between EtOH_550 and FLX induced by $\zeta = -50 \text{ mV} \pm 5$ from the catalyst's interaction with protonated -NH₃⁺ group in pH = 9 (Do et al. 2017). Then, a 32% FLX desorption was confirmed, previously adsorbed, until 5 min, suggesting that the -CF₃ group promoted the molecule repulsions close to the EtOH_550 surface after the initial attraction. After this desorption step, the adsorptive process was retaken,

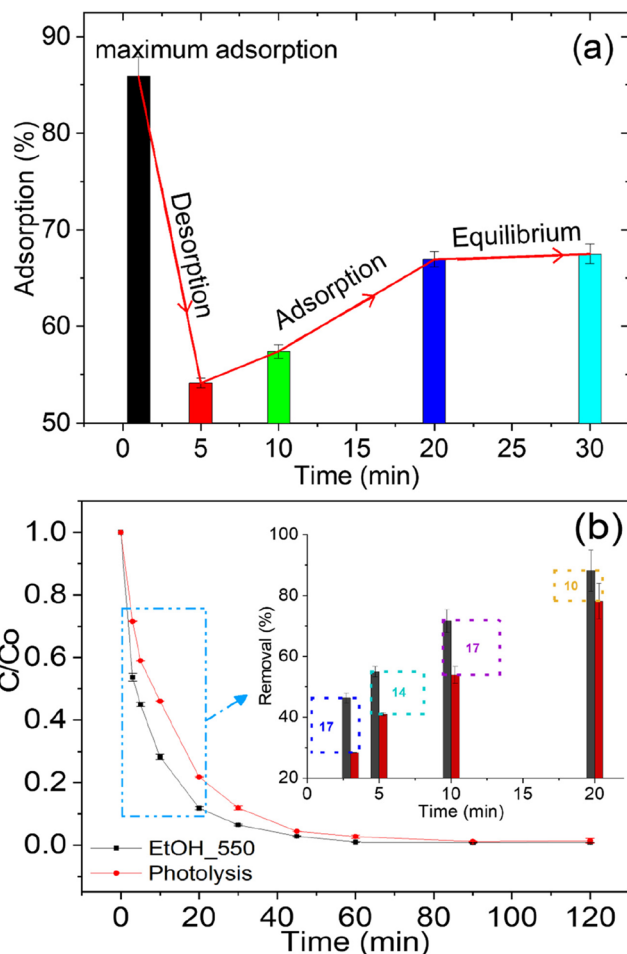


Fig. 8 FLX adsorption in the time interval from 1 to 30 min (a) and decay curve during the photocatalytic process (b)

removing FLX 67% ± 1 in 20 min. Finally, in 30 min, the adsorption was 68% ± 1, showing no variation and, therefore, reaching equilibrium. Thus, before being irradiated, FLX solutions (10 mg L⁻¹) were subjected to adsorption for 30 min.

Figure 8 b showed that up to 30 min, the C/Co ratio decreases considerably for both photochemical processes. Compared with photolytic, the FLX photocatalytic removal showed an average increase of 16% ± 1 for 3, 5, and 10 min. These results corroborate those found during the degradation of the dyes, confirming that EtOH_550 is a photoactive catalyst capable of degrading the different organic pollutants. The chromatographic analyses used to monitor FLX degradation also provided essential details regarding the quantitative by-product formations. According to the literature, TFMP, MAEB, and PPMA are the main by-products formed after the FLX degradation (Moreira et al. 2020a). Therefore, they were quantitatively monitored in the present study.

According to the literature, the conversion from FLX to MAEB + TFMP preferably follows a radical oxidation mechanism. In contrast, the conversion from FLX to PPMA + TFMP complies with the photolytic or hydrogenation

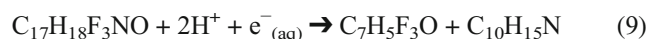
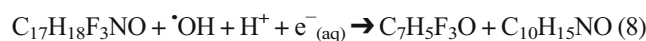
mechanism (Moreira et al. 2020a). Figure 9 a shows the maximum conversion rate obtained during the FLX photolytic and photocatalytic degradations calculated according to the literature (Moreira et al. 2020a). The results confirm that the conversion to TFMP was more significant in both processes precisely because this is present in the two degradation mechanisms. Furthermore, the EtOH_550 catalyst presence did not influence the conversion rate to TFMP, which was similar to that found for the photolytic process. Therefore, this result suggests that the electrostatic repulsion between the -CF₃ group (present in the TFMP structure) and the EtOH_550 ($\zeta = -50 \text{ mV} \pm 5$) prevents the interaction between both, allowing the TFMP to be available in the aqueous phase for a longer time.

The 1:1 stoichiometry is expected for conversion from FLX to MAEB or PPMA (Moreira et al. 2020a). As different routes obtain PPMA or MAEB, the molar ratio between these by-products provides valuable information regarding the

preferential FLX degradation mechanism. Therefore, the molar ratio ($r_{\text{molar}} = (n_{\text{MAEB}}/n_{\text{PPMA}})$) was calculated for the point of greatest conversion rate, where $r_{\text{molar}} = 0.96$ for photolytic removal and $r_{\text{molar}} = 1.5$ for EtOH_550. As the highest r_{molar} value was obtained for EtOH_550, the FLX oxidation mechanism mediated by hydroxyl radicals to preferentially form the MAEB was suggested. A 1.5 mg L^{-1} coumarin solution was irradiated in the absence and presence of the EtOH_550 catalyst to support this idea. The reaction products were monitored by photoluminescence (Fig. 8b). The PL spectra of the samples submitted to photolysis and EtOH_550 showed a peak centered at 452 nm only for the EtOH_550 sample (Fig. 9b).

According to the literature, umbelliferone is the hydroxylation by-product of coumarin responsible at 452 nm PL emitting. However, the emission is not verified in the hydroxyl radical absence (Louit et al. 2005). When adding dimethylsulfoxide (DMSO) as a radical scavenger in the reaction medium, the PL spectra (EtOH_550 + DMSO) showed the peak-centered suppression at 452 nm, confirming that the radicals were not available to umbelliferone form. Therefore, the photoactivity of EtOH_550 when exposed to UV radiation was sufficient to promote electronic excitation and generate the e^- (CB) and h^+ (VB) pairs. These, in turn, were responsible for forming the oxidizing species capable of optimizing the FLX degradation for formed TFMP, PPMA, and MAEB. The by-products formed suggest that the photocatalytic mechanism proposed by Eq. (2) is the preferred one. When acting on the FLX (C₁₇H₁₈F₃NO) degradation, it can be summarized by Eqs. (8) and (9) to explain the TFMP (C₇H₅F₃O), MAEB (C₁₀H₁₅NO), and PPMA (C₁₀H₁₅N) formation.

Thus, the $\cdot\text{OH} + \text{H}^+ + e^-_{(\text{aq})}$ species present in the reaction medium (see Eq. (2)) act in the FLX degradation according to as follows:



This mechanism explains the significant difficulty in degrading FLX compared to RhB or MB, suggesting that while O₂^{•-} or HO₂[•] reactive species are effective in degrading dyes, the same does not occur for the drug degradation, which presents significant persistence to oxidation by these reactive species. Finally, the FLX photocatalytic degradation mechanism in the presence of EtOH_550 can be represented in Fig. 10.

Conclusion

Nb₂O₅ nanofibers were efficiently obtained through the electrospinning technique. Their photocatalytic property was investigated from the degradation of three organic pollutants.

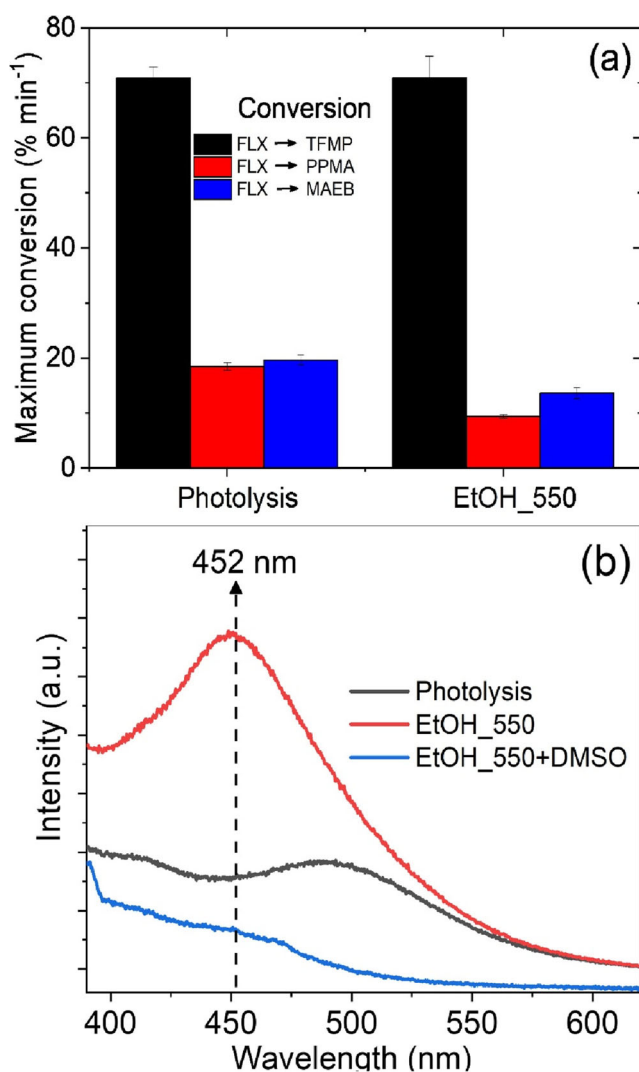


Fig. 9 FLX maximum conversion to by-products (a) and PL spectrum of the umbelliferone formed in the $\cdot\text{OH}$ probe assay (b)

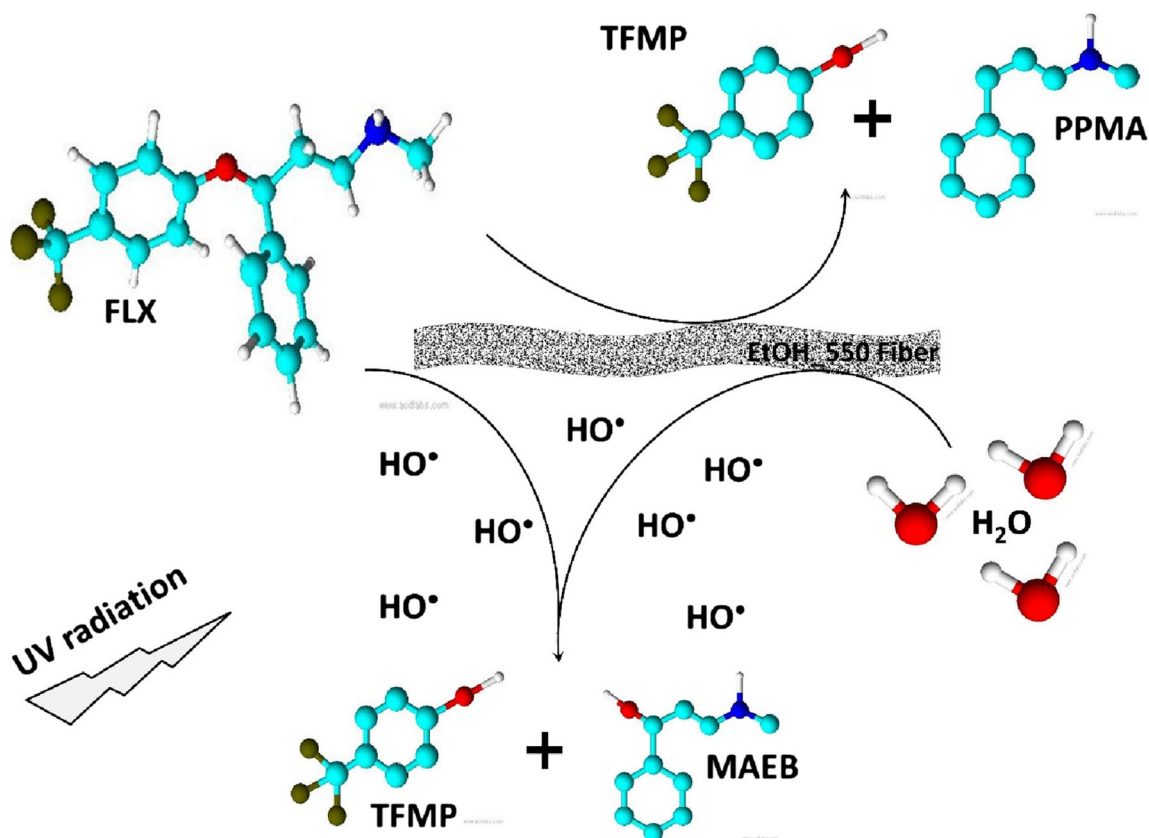


Fig. 10 FLX degradation mechanism mediated by EtOH_550 fiber under UV radiation

XRD and Raman analysis showed that the structure was consistent with the high crystallinity orthorhombic phase (T-Nb₂O₅). The FEG analysis confirmed the ceramic fibers form with a diameter up to 47 nm ± 0.7, and BET results indicate an area up to 85.0 m² g⁻¹ ± 1.7. The broadband PL spectra showed that different energy levels contribute to electronic transition events in the UV-vis region. When applied to RhB or MB photocatalytic degradation, the highest efficiency was obtained for EtOH_550, which degraded 47% ± 2 of RhB in 5 h and 78% ± 1 MB in 1.5 h. The kinetic constant in MB degradation was 86% higher than found for RhB, indicating that the strictly cationic dye was removed with greater efficiency by the catalyst. By investigating different pH conditions during photocatalytic degradation, a removal up to 87% at pH = 3 for RhB (5 h) and 93% for MB at pH = 9 (1.5 h) was achieved, suggesting the chemical nature of the dyes was the responsible factor for guiding photocatalytic efficiency. At pH = 9, the fibers with surface charge could be dispersed in the reaction system with greater efficiency, reaching the optimized condition to degrade the protonated molecules. Besides, due to pK_a = 10.7 and protonated at pH = 9, FLX was subjected to photocatalytic degradation with EtOH_550. For this compound, photocatalysis was up to 17% more efficient than photolysis. From HPLC monitoring of the FLX by-products (TFMP, MAEB, and PPMA), the higher forms of MAEB in the photocatalytic process were consistent with

the formation of hydroxyl radicals in this system. Therefore, Nb₂O₅ nanofibers can be efficiently obtained for application in heterogeneous photocatalysis and can be an alternative material to TiO₂, which is still the most used semiconductor in these systems.

Supplementary Information The online version contains supplementary material available at <https://doi.org/10.1007/s11356-021-15435-8>.

Acknowledgements The authors acknowledge to SisNano/MCTIC, Embrapa (grant # 21.14.03.001.03.00), FAPEMIG (grant # APQ-02823-14), CAPES (grant # 88887.368533/2019-00 and Code # 001), Agronano Network, and FAPEMA (BD – 08822/17).

Availability of data and materials The datasets used and analyzed during the current study are available from the corresponding author on reasonable request.

Author contributions Dr. Edson Tobias de Jesus: writing, methodology; Dr. Ailton José Moreira: writing, methodology; Dr^a Mayara Coelho Sá: methodology; Dr. Gian Paulo Giovanni Freschi: writing—review and editing; Dr^a Myrian Rincón Joya: writing—review and editing; Dr. Máximo Siu Li: review and editing; Dr^a Elaine Cristina Paris: writing, conceptualization, supervision.

Declarations

Ethics approval and consent to participate Not applicable.

Consent for publication Not applicable.

Competing interests The authors declare no competing interests.

References

- Aguilar O, Ángeles C, Castillo CO, Martínez C, Rodríguez R, Ruiz RS, Vizcarra MG (2014) On the ultrasonic degradation of rhodamine B in water: kinetics and operational conditions effect. *Environ Technol (United Kingdom)* 35:1183–1189. <https://doi.org/10.1080/09593330.2013.864711>
- Alves MCF, Souza SC, Silva MRS, Paris EC, Lima SJG, Gomes RM, Longo E, de Souza AG, Garcia dos Santos IM (2009) Thermal analysis applied in the crystallization study of SrSnO₃. *J Therm Anal Calorim* 97:179–183. <https://doi.org/10.1007/s10973-009-0242-x>
- Bian SW, Mudunkotuwa IA, Rupasinghe T, Grassian VH (2011) Aggregation and dissolution of 4 nm ZnO nanoparticles in aqueous environments: Influence of pH, ionic strength, size, and adsorption of humic acid. *Langmuir* 27:6059–6068. <https://doi.org/10.1021/la200570n>
- Choi YI, Kim Y II, Cho DW, et al. (2015) Recyclable magnetic CoFe₂O₄/BiOX (X = Cl, Br and I) microflowers for photocatalytic treatment of water contaminated with methyl orange, rhodamine B, methylene blue, and a mixed dye. *RSC Adv* 5:79624–79634. <https://doi.org/10.1039/c5ra17616f>
- Do TTT, Dao UPN, Bui HT, Nguyen TT (2017) Effect of electrostatic interaction between fluoxetine and lipid membranes on the partitioning of fluoxetine investigated using second derivative spectrophotometry and FTIR. *Chem Phys Lipids* 207:10–23. <https://doi.org/10.1016/j.chemphyslip.2017.07.001>
- Falk G, Borlaf M, López-Muñoz MJ, Fariñas JC, Rodrigues Neto JB, Moreno R (2017) Microwave-assisted synthesis of Nb₂O₅ for photocatalytic application of nanopowders and thin films. *J Mater Res* 32:3271–3278. <https://doi.org/10.1557/jmr.2017.93>
- Fang W, Xing M, Zhang J (2017) Modifications on reduced titanium dioxide photocatalysts: a review. *J Photochem Photobiol C: Photochem Rev* 32:21–39. <https://doi.org/10.1016/j.jphotochemrev.2017.05.003>
- Farooqui HH, Selvaraj S, Mehta A, Heymann DL (2018) Community level antibiotic utilization in India and its comparison vis-à-vis European countries: Evidence from pharmaceutical sales data. *PLoS One* 13:1–12. <https://doi.org/10.1371/journal.pone.0204805>
- Ferreira de EP, Bessa LP, Cardoso VL, Reis MHM (2019) Influence of sintering temperature on the morphology of ceramic hollow fibers prepared from niobium pentoxide. *Int J Appl Ceram Technol* 16: 781–790. doi: <https://doi.org/10.1111/ijac.13118>
- Gorito AM, Ribeiro AR, Almeida CMR, Silva AMT (2017) A review on the application of constructed wetlands for the removal of priority substances and contaminants of emerging concern listed in recently launched EU legislation. *Environ Pollut* 227:428–443. <https://doi.org/10.1016/j.envpol.2017.04.060>
- Gouvêa LFC, Moreira AJ, Freschi CD, Freschi GPG (2018) Speciation of nitrite, nitrate and p-nitrophenol by photochemical vapor generation of NO using High-Resolution Continuum Source Molecular Absorption Spectrometry. *J Food Compos Anal* 70:28–34. <https://doi.org/10.1016/j.jfca.2018.04.003>
- Grenni P, Ancona V, Barra Caracciolo A (2018) Ecological effects of antibiotics on natural ecosystems: a review. *Microchem J* 136:25–39. <https://doi.org/10.1016/j.microc.2017.02.006>
- Grishin AM, Velichko AA, Jalalian A (2013) Nb₂O₅ nanofiber memristor. *Appl Phys Lett* 103:5–10. <https://doi.org/10.1063/1.4817302>
- Gurgel MFC, Moreira ML, Paris EC, Espinosa JWM, Pizani PS, Varela JA, Longo E (2011) BaZrO₃ photoluminescence property: an ab initio analysis of structural deformation and symmetry changes. *Int J Quantum Chem* 111:694–701. <https://doi.org/10.1002/qua.22450>
- Hargreaves JSJ (2016) Some considerations related to the use of the Scherrer equation in powder X-ray diffraction as applied to heterogeneous catalysts. *Catal Struct React* 2:33–37. <https://doi.org/10.1080/2055074X.2016.1252548>
- Hashemzadeh F, Rahimi R, Ghaffarnejad A (2014) Mesoporous nanostructures of Nb₂O₅ obtained by an EISA route for the treatment of malachite green dye-contaminated aqueous solution under UV and visible light irradiation. *Ceram Int* 40:9817–9829. <https://doi.org/10.1016/j.ceramint.2014.02.072>
- Hossain N, Günes O, Zhang C, Koughia C, Li Y, Wen SJ, Wong R, Kasap S, Yang Q (2019) Structural and physical properties of NbO₂ and Nb₂O₅ thin films prepared by magnetron sputtering. *J Mater Sci Mater Electron* 30:9822–9835. <https://doi.org/10.1007/s10854-019-01319-8>
- Joya MR, Barba Ortega JJ, Raba Paez AM, da Silva Filho J, Cavalcante Freire P (2017) Synthesis and characterization of nano-particles of niobium pentoxide with orthorhombic symmetry. *Metals (Basel)* 7: 1–9. <https://doi.org/10.3390/met7040142>
- Khan AA, Tahir M (2019) Recent advancements in engineering approach towards design of photo-reactors for selective photocatalytic CO₂ reduction to renewable fuels. *J CO₂ Util* 29:205–239. <https://doi.org/10.1016/j.jcou.2018.12.008>
- Kostich MS, Batt AL, Lazorchak JM (2014) Concentrations of prioritized pharmaceuticals in effluents from 50 large wastewater treatment plants in the US and implications for risk estimation. *Environ Pollut* 184:354–359. <https://doi.org/10.1016/j.envpol.2013.09.013>
- Kuenemann MA, Szymczyk M, Chen Y, Sultana N, Hinks D, Freeman HS, Williams AJ, Fourches D, Vinuesa NR (2017) Weaver’s historic accessible collection of synthetic dyes: a cheminformatics analysis. *Chem Sci* 8:4334–4339. <https://doi.org/10.1039/c7sc00567a>
- Kumari N, Gaurav K, Samdarshi SK, Bhattacharyya AS, Paul S, Rajbongshi BM, Mohanty K (2020) Dependence of photoactivity of niobium pentoxide (Nb₂O₅) on crystalline phase and electrokinetic potential of the hydrocolloid. *Sol Energy Mater Sol Cells* 208: 110408. <https://doi.org/10.1016/j.solmat.2020.110408>
- Lapworth DJ, Baran N, Stuart ME, Ward RS (2012) Emerging organic contaminants in groundwater: a review of sources, fate and occurrence. *Environ Pollut* 163:287–303. <https://doi.org/10.1016/j.envpol.2011.12.034>
- Lee CM, Palaniandy P, Dahlan I (2017) Pharmaceutical residues in aquatic environment and water remediation by TiO₂ heterogeneous photocatalysis: a review. *Environ Earth Sci* 76. <https://doi.org/10.1007/s12665-017-6924-y>
- Leindecker GC, Alves AK, Bergmann CP (2014) Synthesis of niobium oxide fibers by electrospinning and characterization of their morphology and optical properties. *Ceram Int* 40:16195–16200. <https://doi.org/10.1016/j.ceramint.2014.07.054>
- Leite ER, Paris EC, Longo E, Varela JA (2000) Direct amorphous-to-cubic perovskite phase transformation for lead titanate. *J Am Ceram Soc* 83:1539–1541. <https://doi.org/10.1111/j.1151-2916.2000.tb01427.x>
- Lopes OF, Paris EC, Ribeiro C (2014) Synthesis of Nb₂O₅ nanoparticles through the oxidant peroxide method applied to organic pollutant photodegradation: a mechanistic study. *Appl Catal B Environ* 144: 800–808. <https://doi.org/10.1016/j.apcatb.2013.08.031>
- Louit G, Foley S, Cabillic J, Coffigny H, Taran F, Valleix A, Renault JP, Pin S (2005) The reaction of coumarin with the OH radical revisited: hydroxylation product analysis determined by fluorescence and chromatography. *Radiat Phys Chem* 72:119–124. <https://doi.org/10.1016/j.radphyschem.2004.09.007>
- Machado TR, Sczancoski JC, Beltrán-Mir H, Nogueira IC, Li MS, Andrés J, Cordoncillo E, Longo E (2017) A novel approach to

- obtain highly intense self-activated photoluminescence emissions in hydroxyapatite nanoparticles. *J Solid State Chem* 249:64–69. <https://doi.org/10.1016/j.jssc.2016.12.018>
- Malafatti JOD, Moreira AJ, Sciena CR, Silva TEM, Freschi GPG, Pereira EC, Paris EC (2020) Prozac® removal promoted by HAP:Nb2O5 nanoparticles system: by-products, mechanism, and cytotoxicity assessment. *J Environ Chem Eng* 9:104820. <https://doi.org/10.1016/j.jece.2020.104820>
- McPhie P (2000) Principles of fluorescence spectroscopy, Second ed. Joseph R. Lakowicz. *Anal Biochem* 287:353–354. <https://doi.org/10.1006/abio.2000.4850>
- Merka O, Yarovy V, Bahnemann DW, Wark M (2011) pH-control of the photocatalytic degradation mechanism of rhodamine B over Pb 3 Nb 4 O 13. *J Phys Chem C* 115:8014–8023. <https://doi.org/10.1021/jp108637r>
- Moreira A, Borges A, de Sousa B et al (2018) Photodegradation of fluoxetine applying different photolytic reactors: evaluation of the process efficiency and mechanism. *J Braz Chem Soc* 30:1010–1024. <https://doi.org/10.21577/0103-5053.20180250>
- Moreira AJ, Campos LO, Maldini CP, Dias JA, Paris EC, Giraldo TR, Freschi GPG (2020a) Photocatalytic degradation of Prozac® mediated by TiO2 nanoparticles obtained via three synthesis methods: sonochemical, microwave hydrothermal, and polymeric precursor. *Environ Sci Pollut Res* 27:27032–27047. <https://doi.org/10.1007/s11356-020-08798-x>
- Moreira AJ, Malafatti JOD, Giraldo TR, Paris EC, Pereira EC, de Mendonça VR, Mastelaro VR, Freschi GPG (2020b) Prozac® photodegradation mediated by Mn-doped TiO₂ nanoparticles: evaluation of by-products and mechanisms proposal. *J Environ Chem Eng* 8:104543. <https://doi.org/10.1016/j.jece.2020.104543>
- Nb O, Araújo MA De, Gromboni MF, et al. (2018) Applied catalysis B : environmental contrasting transient photocurrent characteristics for thin films of vacuum-. 237:339–352
- Nico C, Monteiro T, Graça MPF (2016) Niobium oxides and niobates physical properties: review and prospects. *Prog Mater Sci* 80:1–37. <https://doi.org/10.1016/j.pmatsci.2016.02.001>
- Nogueira AE, Lopes OF, Neto ABS, Ribeiro C (2017) Enhanced Cr(VI) photoreduction in aqueous solution using Nb 2 O 5 /CuO heterostructures under UV and visible irradiation. *Chem Eng J* 312:220–227. <https://doi.org/10.1016/j.cej.2016.11.135>
- Nowak I, Jaroniec M (2008) “Hard” vs. “soft” templating synthesis of mesoporous Nb2O5 catalysts for oxidation reactions. *Top Catal* 49: 193–203. <https://doi.org/10.1007/s11244-008-9084-1>
- Obregón S, Colón G (2013) On the different photocatalytic performance of BiVO4 catalysts for methylene blue and rhodamine B degradation. *J Mol Catal A Chem* 376:40–47. <https://doi.org/10.1016/j.molcata.2013.04.012>
- Oliveira LH, Paris EC, Avansi W, Ramirez MA, Mastelaro VR, Longo E, Varela JA (2013) Correlation between photoluminescence and structural defects in Ca 1+x Cu 3 - X Ti 4 O 12 systems. *J Am Ceram Soc* 96:209–217. <https://doi.org/10.1111/jace.12020>
- Paris EC, Espinosa JWM, de Lazaro S, Lima RC, Joya MR, Pizani PS, Leite ER, Souza AG, Varela JA, Longo E (2007) Er³⁺ as a marker for order-disorder determination in the PbTiO₃ system. *Chem Phys* 335:7–14. <https://doi.org/10.1016/j.chemphys.2007.03.019>
- Paris EC, Gurgel MFC, Joya MR, Casali GP, Paiva-Santos CO, Boschi TM, Pizani PS, Varela JA, Longo E (2010) Structural deformation monitored by vibrational properties and orbital modeling in (Pb, Sm)TiO₃ systems. *J Phys Chem Solids* 71:12–17. <https://doi.org/10.1016/j.jpcs.2009.09.012>
- Paris EC, Malafatti JOD, Sciena CR, Junior LFN, Zenatti A, Escote MT, Moreira AJ, Freschi GPG (2020) Nb2O5 nanoparticles decorated with magnetic ferrites for wastewater photocatalytic remediation. *Environ Sci Pollut Res* 28:23731–23741. <https://doi.org/10.1007/s11356-020-11262-5>
- Petrie B, Barden R, Kasprzyk-Hordern B (2015) A review on emerging contaminants in wastewaters and the environment: current knowledge, understudied areas and recommendations for future monitoring. *Water Res* 72:3–27. <https://doi.org/10.1016/j.watres.2014.08.053>
- Pi Y, Li X, Xia Q, Wu J, Li Y, Xiao J, Li Z (2018) Adsorptive and photocatalytic removal of persistent organic pollutants (POPs) in water by metal-organic frameworks (MOFs). *Chem Eng J* 337: 351–371. <https://doi.org/10.1016/j.cej.2017.12.092>
- Pinheiro BS, Gimenes LLS, Moreira AJ et al (2016) Arsenic speciation in environmental samples using different acid concentrations and ultrasonic extraction for the determination by HG-FAAS. *At Spectrosc* 37:83–89
- Qi S, Zuo R, Liu Y, Wang Y (2013) Synthesis and photocatalytic activity of electrospun niobium oxide nanofibers. *Mater Res Bull* 48:1213–1217. <https://doi.org/10.1016/j.materresbull.2012.11.074>
- Raba AM, Barba-Ortega J, Joya MR (2015) The effect of the preparation method of Nb2O5 oxide influences the performance of the photocatalytic activity. *Appl Phys A Mater Sci Process* 119:923–928. <https://doi.org/10.1007/s00339-015-9041-3>
- Radoń A, Łoński S, Warski T, Babilas R, Tański T, Dudziak M, Łukowicz D (2019) Catalytic activity of non-spherical shaped magnetite nanoparticles in degradation of Sudan I, rhodamine B and methylene blue dyes. *Appl Surf Sci* 487:1018–1025. <https://doi.org/10.1016/j.apsusc.2019.05.091>
- Rauf MA, Ashraf SS (2009) Fundamental principles and application of heterogeneous photocatalytic degradation of dyes in solution. *Chem Eng J* 151:10–18. <https://doi.org/10.1016/j.cej.2009.02.026>
- Reeta Mary I, Sonia S, Navadeepthy D, Mangalaraj D, Viswanathan C, Ponpandian N (2018) Surfactant-free solvothermal synthesis of hydroxyapatite nested bundles for the effective photodegradation of cationic dyes. *J Phys Chem Solids* 116:180–186. <https://doi.org/10.1016/j.jpcs.2018.01.035>
- Rtimi S, Kiwi J, Karimi A, Sanjinés R (2018) Innovative Ti 1– x Nb x N– Ag films inducing bacterial disinfection by visible light/thermal treatment. *ACS Appl Mater Interfaces* 10:12021–12030. <https://doi.org/10.1021/acsami.7b19225>
- Sanaullah M, Usman M, Wakeel A, Cheema SA, Ashraf I, Farooq M (2020) Terrestrial ecosystem functioning affected by agricultural management systems: a review. *Soil Tillage Res*:196. <https://doi.org/10.1016/j.still.2019.104464>
- Shao R, Cao Z, Xiao Y, Dong H, He W, Gao Y, Liu J (2014) Enhancing photocatalytic activity by tuning the ratio of hexagonal and orthorhombic phase Nb2O5 hollow fibers. *RSC Adv* 4:26447–26451. <https://doi.org/10.1039/c4ra02038c>
- Shen R, Jiang C, Xiang Q, Xie J, Li X (2019) Surface and interface engineering of hierarchical photocatalysts. *Appl Surf Sci* 471:43–87. <https://doi.org/10.1016/j.apsusc.2018.11.205>
- Silva GTST, Nogueira AE, Oliveira JA et al (2019) Acidic surface niobium pentoxide is catalytic active for CO 2 photoreduction. *Appl Catal B Environ* 242:349–357. <https://doi.org/10.1016/j.apcatb.2018.10.017>
- Stern EA (1978) Structure determination by X-ray absorption. *Contemp Phys* 19:289–310. <https://doi.org/10.1080/00107517808210887>
- Védrine JC (2019) Importance, features and uses of metal oxide catalysts in heterogeneous catalysis. *Chin J Catal* 40:1627–1636. [https://doi.org/10.1016/S1872-2067\(18\)63162-6](https://doi.org/10.1016/S1872-2067(18)63162-6)
- Wang C, Zhang Y, Yu L, Zhang Z, Sun H (2013) Oxidative degradation of azo dyes using tourmaline. *J Hazard Mater* 260:851–859. <https://doi.org/10.1016/j.jhazmat.2013.06.054>
- Wang K, Xu J, Hua X, Li N, Chen M, Teng F, Zhu Y, Yao W (2014) Highly efficient photodegradation of RhB-MO mixture dye wastewater by Ag3PO4 dodecahedrons under acidic condition. *J Mol Catal A Chem* 393:302–308. <https://doi.org/10.1016/j.molcata.2014.06.026>

- Zeng GY, Wang H, Guo J, Cha LM, Dou YH, Ma JM (2017) Fabrication of Nb₂O₅/C nanocomposites as a high performance anode for lithium ion battery. *Chin Chem Lett* 28:755–758. <https://doi.org/10.1016/j.ccllet.2017.01.001>
- Zhao J, Xu H, Tang D, Mathews JP, Li S, Tao S (2016) A comparative evaluation of coal specific surface area by CO₂ and N₂ adsorption and its influence on CH₄ adsorption capacity at different pore sizes. *Fuel* 183:420–431. <https://doi.org/10.1016/j.fuel.2016.06.076>
- Zhou X, Li Z, Wang Y, Sheng X, Zhang Z (2008) Photoluminescence of amorphous niobium oxide films synthesized by solid-state reaction. *Thin Solid Films* 516:4213–4216. <https://doi.org/10.1016/j.tsf.2007.12.112>
- Zhuang XJ, Xia QN, Wang YQ, Tsang SCE, Gong XQ (2016) Hydrodeoxygenation of butyric acid at multi-functional Nb₂O₅ catalyst: a density functional theory study. *Int J Hydrog Energy* 41:18502–18508. <https://doi.org/10.1016/j.ijhydene.2016.08.220>

Publisher's note Springer Nature remains neutral with regard to jurisdictional claims in published maps and institutional affiliations.